frontiers | Frontiers in Materials

TYPE Original Research
PUBLISHED 16 October 2025
DOI 10.3389/fmats.2025.1684414

OPEN ACCESS

EDITED BY
Mazeyar Parvinzadeh Gashti,
Pittsburg State University, United States

REVIEWED BY
Mahmoud Abbasi,
University of Kashan, Iran
Yopi,
Yusuf Tanoto, Petra Christian
University, Indonesia
M. Zamri Yusop,
University of Technology Malaysia, Malaysia

*CORRESPONDENCE
Sherzod Kurbanbekov,
sherzod.kurbanbekov@ayu.edu.kz

RECEIVED 12 August 2025
ACCEPTED 29 September 2025
PUBLISHED 16 October 2025

CITATION
Aidarova M, Kurbanbekov S, Kizatov A, Urkunbay A, Bayatanova L, Rutkowska-Gorczyca M and Amangeldiyeva Y (2025) Influence of milling time and binder composition on phase evolution in WC-based composite powders fabricated via high-energy ball milling.
Front. Mater. 12:1684414.
doi: 10.3389/fmats.2025.1684414

Influence of milling time and binder composition on phase evolution in WC-based composite powders fabricated via high-energy ball milling

Madina Aidarova[1], Sherzod Kurbanbekov[1,2]*, Aibar Kizatov[1], Azamat Urkunbay[1], Lyaila Bayatanova[1], Małgorzata Rutkowska-Gorczyca[3] and Yulduz Amangeldiyeva[1,2]

[1]Center of Excellence "VERITAS", NJSC D. Serikbayev East Kazakhstan Technical University, Ust-Kamenogorsk, Kazakhstan, [2]LLP "Institute of Innovative Technologies and New Materials", Turkestan, Kazakhstan, [3]Department of Vehicle Engineering, Faculty of Mechanical Engineering, Wroclaw University of Science and Technology, Wroclaw, Poland

Cobalt-free WC-(Fe/Ni) composite powders were evaluated as practical alternatives to WC-Co, with emphasis on how the post-milling powder state governs downstream processing. Blends of 88 wt% WC-12 wt% Fe, 88 wt% WC-12 wt% Ni, and 88 wt% WC-6 wt% Fe-6 wt% Ni were ball-milled for 0–4 h at 500 rpm in Ar. Phase constitution was assessed by X-ray diffraction; crystallite size and microstrain were quantified by Williamson-Hall/Scherrer; particle-size distributions (PSD) were measured by laser diffraction and benchmarked against SEM. Across all series, WC and metallic binder were retained while W_2C/W remained at trace levels (<1%). In WC-FeNi, the free-Ni fraction decreased (1.9 →0.5%) and Fe increased (9.5 →23.6%), indicating formation of an Fe(Ni) solid solution during milling. WC crystallites refined from ~50-55 nm to 22.6 nm (WC-Fe), 20.7 nm (WC-Ni), and 21.1 nm (WC-FeNi) by 4 h, with most refinement achieved within 0–2 h. In parallel, PSD shifted to larger particle sizes due to cold welding: D50 increased 3.40 →10.30 μm (Fe), 2.87 →7.27 μm (Ni), and 4.11 →7.42 μm (FeNi), while PSD/SEM jointly evidenced multigrain aggregates in the 5–10 μm range. This establishes an inverse micro/nano linkage wherein agglomerates coarsen as WC crystallites refine. Among the chemistries, WC-FeNi at 1–2 h provided the most balanced outcome ~21 nm crystallites, moderate microstrain, and limited D50 growth defining a preferred window for uniform compaction and sintering. These results clarify processing–structure relations in cobalt-free WC composites and outline a short-duration milling strategy to engineer powder-state attributes for improved sinterability.

KEYWORDS

WC-based composites, mechanosynthesis, high-energy ball milling, W_2C formation, X-ray diffraction (XRD), Williamson-Hall analysis, SEM/EDS mapping, particle-size distribution

1 Introduction

WC-based cemented carbides are among the most sought-after materials for the manufacture of cutting and wear-resistant tools owing to their combination of high hardness, resistance to abrasive wear, and stability at elevated temperatures (Kumar et al., 2023; Gao et al., 2020; García et al., 2019). Traditionally, Co (≈80% of the global market) serves as the primary binder phase in such composites (Zeiler, 2019; Lyu et al., 2020). However, its widespread use is associated with serious limitations: the high cost and scarcity of cobalt, the toxicity of its compounds and related health risks, as well as dependence on a limited number of supplier countries. Taken together, these factors stimulate the search for cobalt-free alternatives that can match WC-Co in performance characteristics while meeting contemporary requirements for environmental sustainability and sustainable production (Lyu et al., 2020; Ravotti et al., 2024).

In recent years, attention has turned to iron- and nickel-based binder phases, as well as their alloys, which exhibit good wetting of WC, favorable processing characteristics, and substantially lower environmental and economic burdens (Fathipour et al., 2024; Krawitz and Drake, 2015; Yang et al., 2020). Theoretical studies indicate that the interfacial bonding energy at the W-Fe interface is higher than at W-Co and W-Ni, confirming the potential of Fe to increase grain-boundary strength (Sun et al., 2020; Smetanina et al., 2023; Shichalin et al., 2020; Gruber et al., 2023). When Fe and Ni are used together, the binder phase can be further stabilized by combining the oxidation resistance of Ni with (Rong et al., 2012) the strength provided by Fe. In addition, the resulting γ-phase (Fe-Ni solid solution) promotes a more uniform distribution of residual stresses and increases the ductility of the composite (Li et al., 2024; Lima et al., 2024; Sten et al., 2025; Jayaraj et al., 2023; Cramer et al., 2020; Steinlechner et al., 2022). Nevertheless, research in this area remains fragmented and is focused predominantly on coatings. For example, Tahaei et al. optimized plasma-transferred arc (PTA) parameters for WC–Ni coatings on tool steel and identified characteristic microstructures comprising an Fe-Ni-Cr dendritic matrix together with WCrC and WC carbides (Tahaei et al., 2023; Tahaei et al., 2024). Similarly, Abbasi et al. investigated the addition of WC nanoparticles to Ni-WC coatings and observed γ-Ni dendrites with interdendritic Ni-Fe eutectics and $(Fe,Cr)_7C_3$ carbides (Abbasi et al., 2024). These results confirm the efficacy of Ni- and Fe-bonded systems; however, the alloys exhibit different chemical reactivities: Fe readily forms brittle η-type phases such as $(Fe,W)_6C$ and W_2C with even slight deviations in carbon balance, whereas Ni is generally inert toward WC (Lantcev et al., 2021; Lantsev et al., 2021). Consequently, such studies are largely confined to surface hardfacing and do not address fundamental aspects of powder-precursor formation for cemented carbides.

A key shortcoming of current approaches is that the earliest stages of structure formation during high-energy ball milling and mechanosynthesis are scarcely explored. Yet it is precisely in this period that the foundations of the final microstructure are laid: oxide films are disrupted, defects are generated, metastable states can emerge, and the binder phase may undergo amorphization. Systematic, comparative studies of WC-Fe, WC-Ni, and WC-FeNi systems at the milling stage are absent from the literature, leaving a gap in understanding the mechanisms of structural evolution in cobalt-free composites. The present work addresses this gap by examining the effects of milling time and binder composition (Fe, Ni, Fe-Ni) on phase evolution and structural characteristics

TABLE 1 Modes for Mechanosynthesis WC-FeNi, WC-Fe, WC-Ni and composition of powder mixture.

Sample name	Unique code	Time, hour	Surfactant additive (stearic acid), wt%	Rotation speed, rpm	Atmosphere	Mass ratio (ball/powder)
Powder mixture blending	a	0,3	-	200	Argon	10:1
Mechanosynthesis						
88 wt% WC - 12 wt.%Fe	b_1	1	2.5	500	Argon	10:1
	c_1	2				
	d_1	4	3			
88 wt% WC - 12 wt% Ni	b_2	1	2.5			
	c_2	2				
	d_2	4	3			
88 wt% WC - 6 wt% Fe + 6 wt% Ni	b_3	1	2.5			
	c_3	2				
	d_3	4	3			

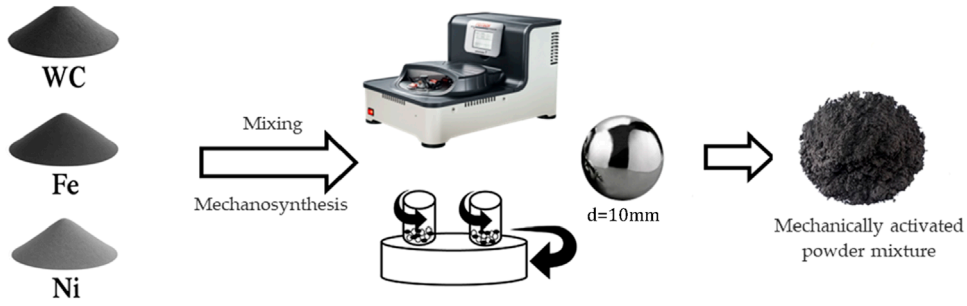

FIGURE 1
Schematic of the mechanosynthesis process for WC-based powders.

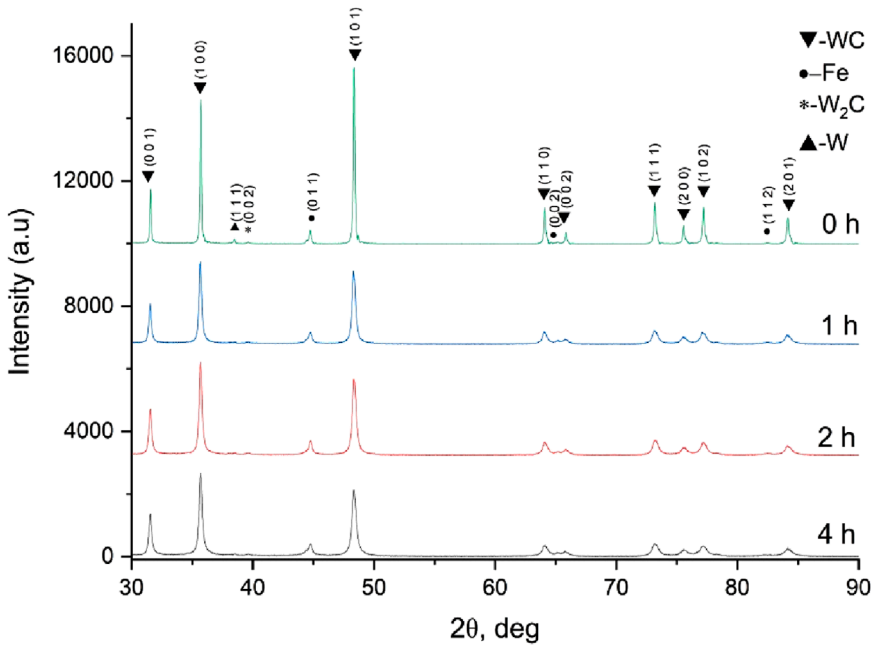

FIGURE 2
XRD patterns of the 88 wt% WC-12 wt% Fe powder mixture at different mechanosynthesis times (0, 1, 2, and 4 h).

TABLE 2 Phase composition of WC-Fe powder mixture depending on milling time.

Time, h	WC, %	Fe, %	W_2C, %	W, %
0	85.3	14.5	0.5	0.2
1	80.9	18.7	0.4	0.1
2	81.5	18.0	0.4	0.1
4	76.7	22.9	0.3	0.1

of WC-based composites. In contrast to the numerous coating studies, the emphasis here is on pre-sintering powder states that subsequently govern cemented-carbide properties. The results provide a foundation for developing WC-FeNi composites as a practical and environmentally safer alternative to WC-Co for next-generation cobalt-free cemented carbides.

2 Materials and methods

The powder blends investigated in this work were prepared from elemental WC, Fe, and Ni powders with particle sizes <50 μm and 99% purity, supplied by Hebei Suoyi New Material Technology (Hebei Province, China). According to the supplier's datasheet, the as-received powders had particle sizes below 30 μm. The use of micron-sized tungsten carbide powder was motivated by the need to form a fine-grained structure capable of enhancing the strength characteristics of the resulting cemented carbides.

Three compositions with different binder chemistries were compared: WC-12 wt% Fe, WC-12 wt% Ni, and WC-6 wt% Fe + 6 wt% Ni. Each blend contained 88 wt% WC and a metallic binder

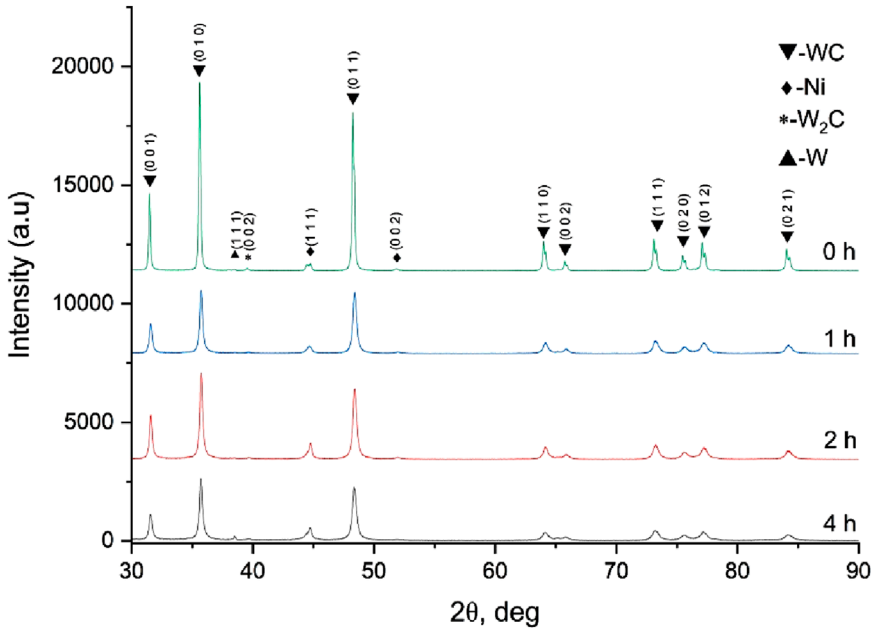

FIGURE 3
XRD patterns of the 88 wt% WC-12 wt% Ni powder mixture at different mechanosynthesis times (0, 1, 2, and 4 h).

TABLE 3 Phase composition of WC-Ni powder mixture depending on milling time.

Time, h	WC, %	Ni, %	W_2C, %	W, %
0	88.8	10.3	0.6	0.3
1	81.5	18.1	0.3	0.1
2	80.5	19.1	0.3	0.1
4	79.2	20.5	0.2	0.1

phase. These specific compositions were selected to keep the total binder content constant at 12 wt% (typical for cemented carbides) while varying the binder chemistry. Such a binder level provides sufficient strength without a substantial decrease in hardness. Comparing Fe-only and Ni-only binders isolates their individual effects (Fe tends to form η-carbides, whereas Ni generally suppresses carbide formation), while the 6% Fe-6% Ni combination enables assessment of potential synergy in which Ni can mitigate Fe-related brittleness and Fe can enhance the strength associated with Ni. Each powder mixture was labeled and prepared under identical conditions. The mechanosynthesis conditions used in the experiments are given in Table 1.

Prior to high-energy milling, accurately weighed WC, Fe, and Ni powders were charged into stainless-steel grinding bowls with stainless-steel balls and premixed for 20 min at 200 rpm to promote initial homogeneity. For mechanosynthesis, ~9 g of the premix was loaded into a 45 mL stainless-steel vial with 10 mm stainless-steel balls at a ball-to-powder mass ratio (BPR) of 10:1 inside an argon-filled glovebox (VGB-3C) to prevent oxidation. The vial was hermetically sealed and mounted on a planetary micro mill (Pulverisette 7 premium line, Fritsch GmbH, Germany). Milling was conducted at 500 rpm. This speed was selected, based on literature guidance, as optimal for efficient mechanical alloying without excessive cold welding or ignition; it provides a high-energy impact regime suitable for particle fragmentation and alloying while keeping the temperature within a safe range.

The influence of milling time on the structural characteristics of WC-FeNi/Fe/Ni elemental powder blends was assessed at durations of 1, 2, and 4 h. Stearic acid was employed as a PCA and added at 2.5 wt% and 3 wt% relative to the total solids. The higher PCA concentration at longer milling times was intended to counteract the increased risk of particle agglomeration and to ensure continuous dispersion of the metallic constituents within the WC matrix. In addition to suppressing cold welding, the PCA promotes a uniform distribution of the metallic species in the carbide matrix, stabilizes the resulting dispersed system, and helps maintain a fine, homogeneous structurecritical for subsequent compaction and sintering. Increasing the stearic acid content to 3 wt% is justified for extended processing, where the collision energy already provides sufficient activation.

The entire process is illustrated schematically in Figure 1, which depicts the sequence from powder selection and mixing to high-energy milling and final production of mechanically activated composite powders.

Surface morphology was studied using high-resolution scanning electron microscopy (SEM, Tescan Mira, Czech Republic). The obtained micrographs enabled visualization of particle aggregation and shape characteristics. The phase composition of the samples was determined by X-ray diffraction (XRD) using a diffractometer (X'PertPRO, Malvern Panalytical Empyrean, Netherlands) equipped with a copper (Cu) anode ($K\alpha_2$ wavelength = 1.54443 Å), operating

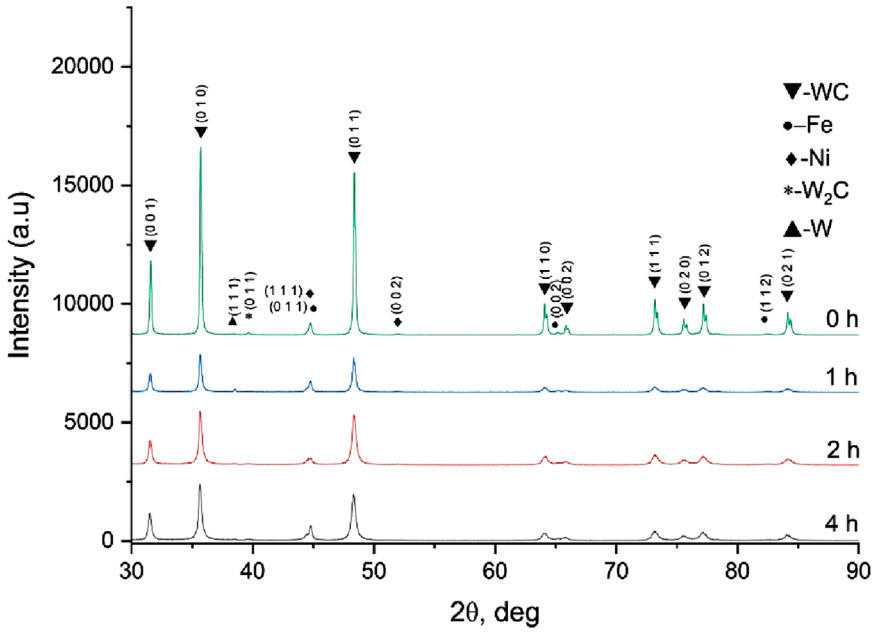

FIGURE 4
XRD patterns of the 88 wt% WC-6 wt% Fe-6 wt% Ni powder mixture at different mechanosynthesis times (0, 1, 2, and 4 h).

TABLE 4 Phase composition of WC- FeNi powder mixture depending on milling time.

Time, h	WC, %	Fe, %	Ni, %	W_2C, %	W, %
0	87.8	9.5	1.9	0.6	0.3
1	71.0	19.0	9.0	0.3	0.7
2	80.9	17.2	1.2	0.4	0.4
4	75.3	23.6	0.5	0.3	0.2

TABLE 5 Crystallite sizes (nm) as a function of milling time.

Samples	0 h (mixing)	1 h	2 h	4 h
88 wt% WC – 12 wt% Fe	54.5	31.9	25.5	22.6
88 wt% WC – 12 wt% Ni	53.3	24.3	23.9	20.7
88 wt% WC – 6 wt% Fe – 6 wt% Ni	51.6	33.6	21.5	21.1

in continuous scanning mode over a 2θ range of 20°–90°, with a step size of 0.0200° and generator settings of 40 mA and 45 kV. To quantitatively assess the structural changes in the material resulting from mechanical activation, the crystallite sizes of the main phases were calculated. The crystallite size was determined using mathematical calculations based on the Scherrer equation:

$$D = \frac{K\lambda}{\beta \cos\theta}$$

where D is the crystallite size (nm), K is the shape factor (taken as 0.9), λ is the X-ray wavelength (0.15444 nm for Cu Kα radiation), β is the full width at half maximum (FWHM) of the diffraction peak (in radians), and θ is the Bragg angle (in radians) (Scherrer, 1918).

Williamson Hall Method (UDM). To estimate the average crystallite size D and lattice microstrain ε, plots of β_{hkl} cos θ versus 4 sin θ were constructed using a set of non-overlapping WC reflections. The peak breadth β_{hkl} was taken as the FWHM in 2θ (in radians) after substracting if the contribution (Cullity, 1986),

$$\beta = \sqrt{\beta_{obc}^2 - \beta_{inst}^2}$$

Linear regression was performed without weighting (No weighting) using the model $y = a + bx$, where $y = \beta_{hkl} \cos\theta$ and $x = 4 \sin\theta$. The following equation was used (Williamson and Hall, 1953):

$$\beta_{hkl} \cos\theta = \frac{K\lambda}{D} + 4\varepsilon \sin\theta$$

where K = 0.9 (shape factor) and λ is the X-ray wavelength (Cu Kα, λ = 1.5406 Å). The parameters were obtained as

$$D = \frac{K\lambda}{D},\ \varepsilon = \frac{b}{4}$$

The peak widths were determined by fitting Gaussian functions using the HighScore software. The (101) peak of the WC phase was used for all calculations to maintain consistency across the samples. The peak broadening values (β) were determined by fitting the diffraction profiles with Gaussian functions using HighScore Plus software (Malvern Panalytical). Instrumental broadening was corrected by subtracting the FWHM of a standard Si sample measured under identical conditions. This methodology enables the evaluation of crystallite refinement induced by mechanical

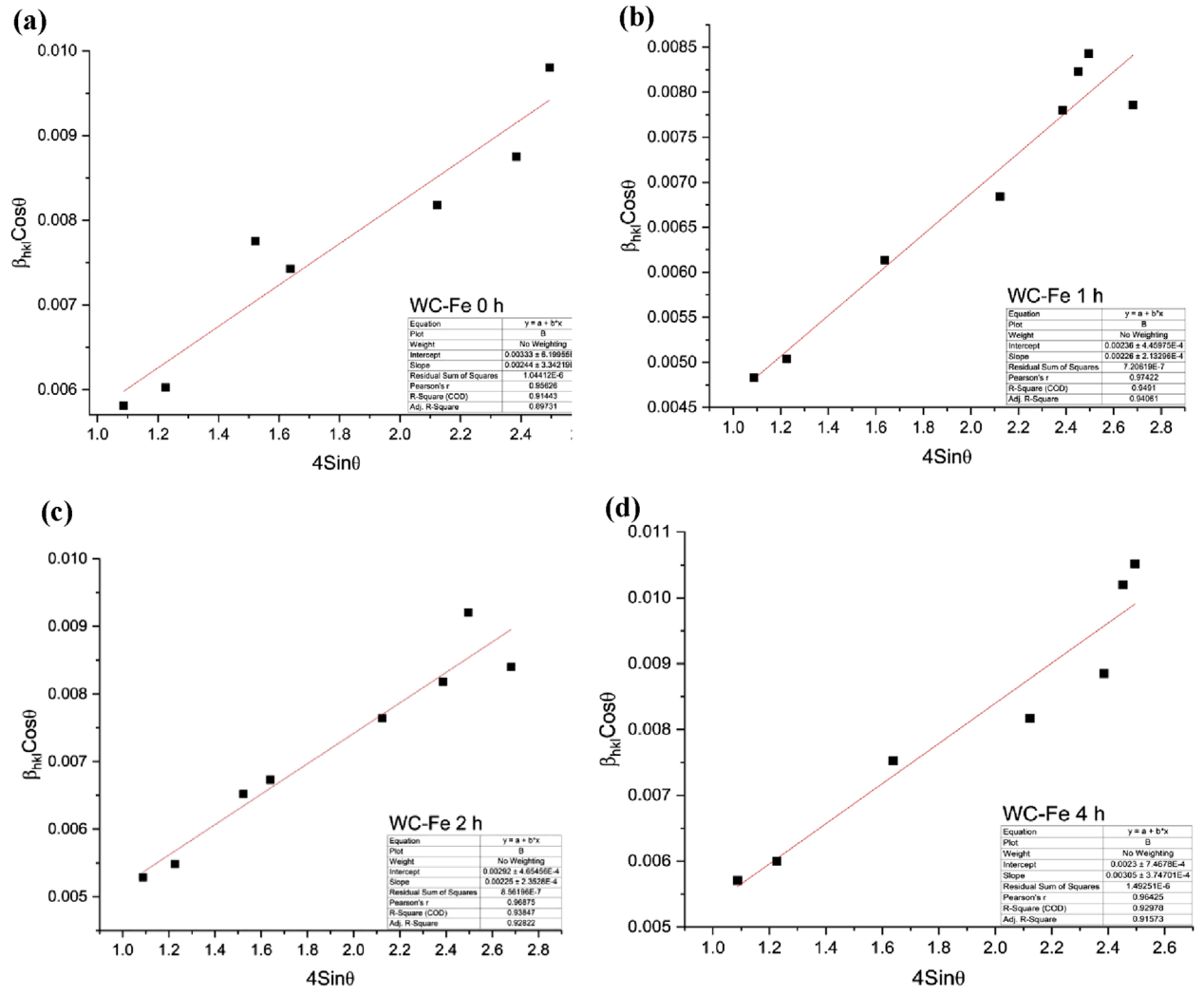

FIGURE 5
Williamson-Hall plots for WC-Fe powder mixture at different milling times **(a)** 0 h, **(b)** 1 h, **(c)** 2 h, and **(d)** 4 h.

activation, providing insights into the microstructural evolution of the powders.

The particle size distribution of the powders was measured using laser diffraction with an automated particle size analyzer (Analysette-22 NeXT Nano, Fritsch, Germany), based on the principles of measuring the intensity of scattered radiation induced by particles of various diameters. Measurements were carried out in a liquid dispersion medium with ultrasonic treatment to break up agglomerates and obtain a representative distribution.

3 Results

3.1 Phase composition (XRD analysis)

X-ray diffraction data in Figure 2 show the phase constitution of the WC–Fe sample subjected to mechanical alloying for 0, 1, 2, and 4 h. The identified phases are WC (PDF 98-001–5406), W_2C (PDF 98-007–7567), W (PDF 98-004–1521), and Fe (PDF 98-063–1724). A gradual decrease in the fraction of crystalline WC is observed (from ~85% to ~76.7% of the total identified phases) accompanied by a corresponding increase in the apparent fraction of metallic Fe (from ~14.5% to ~22.9%) as milling time increases from 0 to 4 h (Table 2). At the initial stage (0 h), the diffractogram exhibits intense peaks characteristic of hexagonal WC, with dominant reflections from (001), (100), (101), (110), and (102), along with a small amount of α-Fe (bcc). Minor lines from W_2C and W are present in all starting blends, which may originate from impurities in the as-received WC. Concurrently, the intensity of the Fe (110) reflection decreases and broadens, indicating that the ductile Fe binder becomes dispersed into nanometer-scale regions within the composite. The presence of W_2C in the Fe-bonded sample points to partial decarburization of WC under intensive milling. This is attributed to the tendency of the iron binder to react with carbon from WC, leading to carbon deficiency in the carbide phase. The literature reports that Fe-bonded systems readily form η-phase carbides (of the M_6C or $M_{12}C$ types, e.g., Fe_3W3C) under carbon-deficient conditions; therefore, careful carbon balancing is required to avoid excessive η-phase in

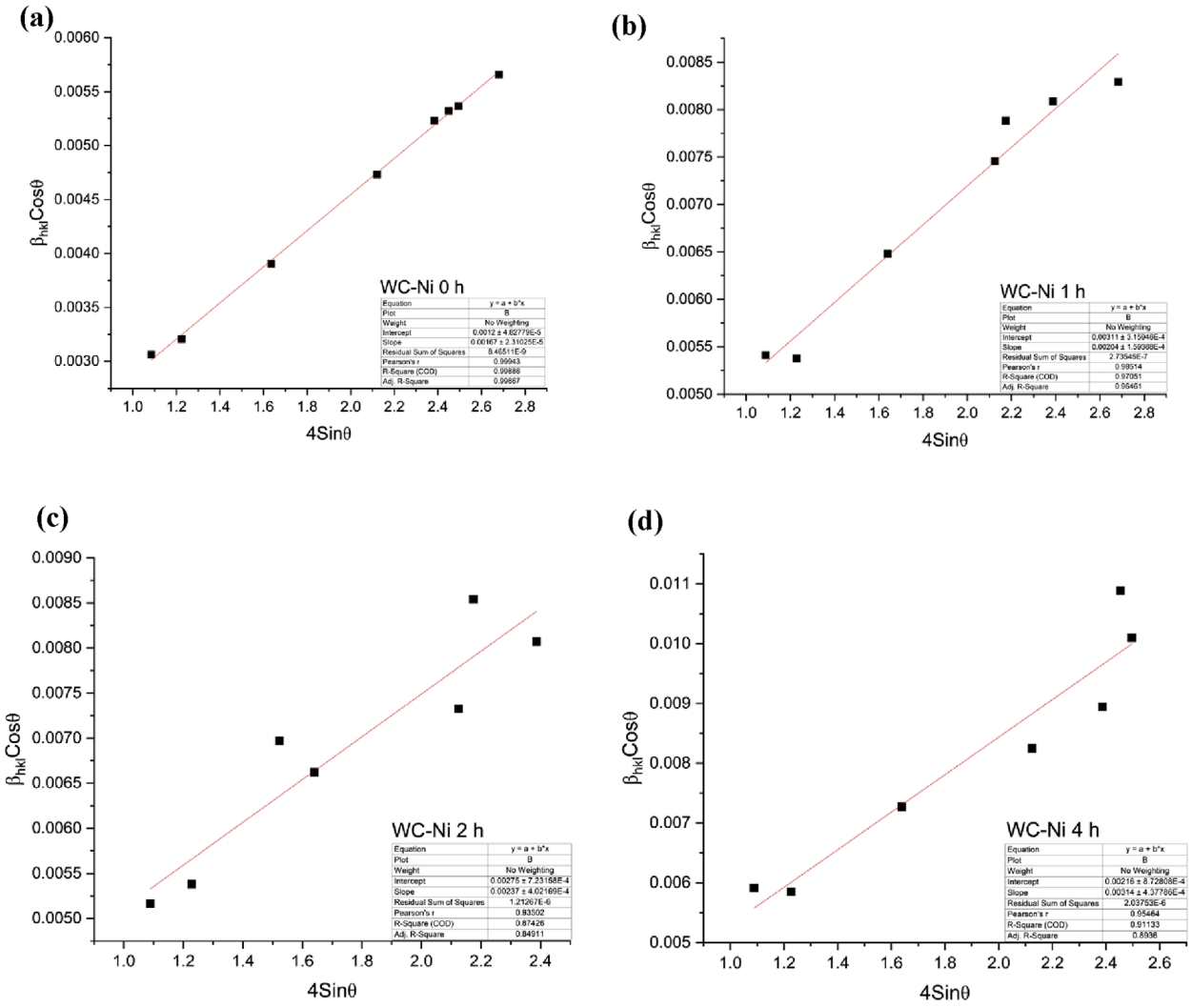

FIGURE 6
Williamson-Hall plots for WC-Ni powder mixture at different milling times **(a)** 0 h, **(b)** 1 h, **(c)** 2 h, and **(d)** 4 h.

WC-based composites with an iron binder, as an excess can embrittle the material (Hoier et al., 2017).

XRD patterns of the 88 wt% WC-12 wt% Ni powder blend are shown in Figure 3. In the as-mixed state (0 h), intense reflections of hexagonal WC-similar to the previous system are observed, together with weak Ni peaks featuring the characteristic (111) reflection. The identified phases comprise WC (PDF 98-001–5406), W_2C (PDF 98-007–7567), W (PDF 98-004–1521), and Ni (PDF 98-004–3397). The WC fraction decreases from ~88.8% to ~79.2%, while the Ni phase fraction increases from ~10.3% to ~20.5% (Table 3). With increasing milling time, progressive broadening of WC reflections is evident, and Ni peaks also broaden after 2 and 4 h of processing, indicating possible incorporation of Ni into defect-rich intergranular regions at WC grain boundaries (and/or crystallite refinement with associated microstrain). WC is structurally more resistant to decarburization in the presence of Ni. The apparent enrichment of the X-ray-detectable metallic phase points to a redistribution of crystallinity: a reduced contribution from coarse-crystalline WC (in part transitioning to a fine-crystalline state). The absence of new peaks in the diffractograms likewise indicates that Ni-W intermetallics (or a Ni-rich η-phase such as $(Ni,W)_3C$) do not form during milling; their formation typically requires higher temperatures.

XRD patterns for the WC-FeNi composite (Figure 4) exhibit milling behavior that is in many respects intermediate between the Fe-only and Ni-only cases, yet with distinctive features arising from Fe–Ni interactions. The identified phases are WC (PDF 96-150–1519), W_2C (PDF 98-007–7567), W (PDF 98-004–1521), Fe (PDF 98-063–1724), and Ni (PDF 98-004–3397). In the as-mixed state (0 h), WC, Fe, and Ni are resolved separately at ~87.8 wt% WC, ~9.5 wt% Fe, and ~1.9 wt% Ni (Table 4). After 1 h of milling, the Fe and Ni peaks broaden and shift slightly. By 2 h, the amount of free Ni drops sharply (<2 wt%). After 4 h, individual Fe and Ni peaks are no longer clearly resolved; instead, a single broad feature appears near 44°–45° 2θ. This evolution suggests that Fe and Ni become highly intermixed or alloyed. Because Fe and Ni are mutually soluble, severe deformation during milling can promote formation of an Fe-Ni solid solution. Although room-temperature alloying is limited,

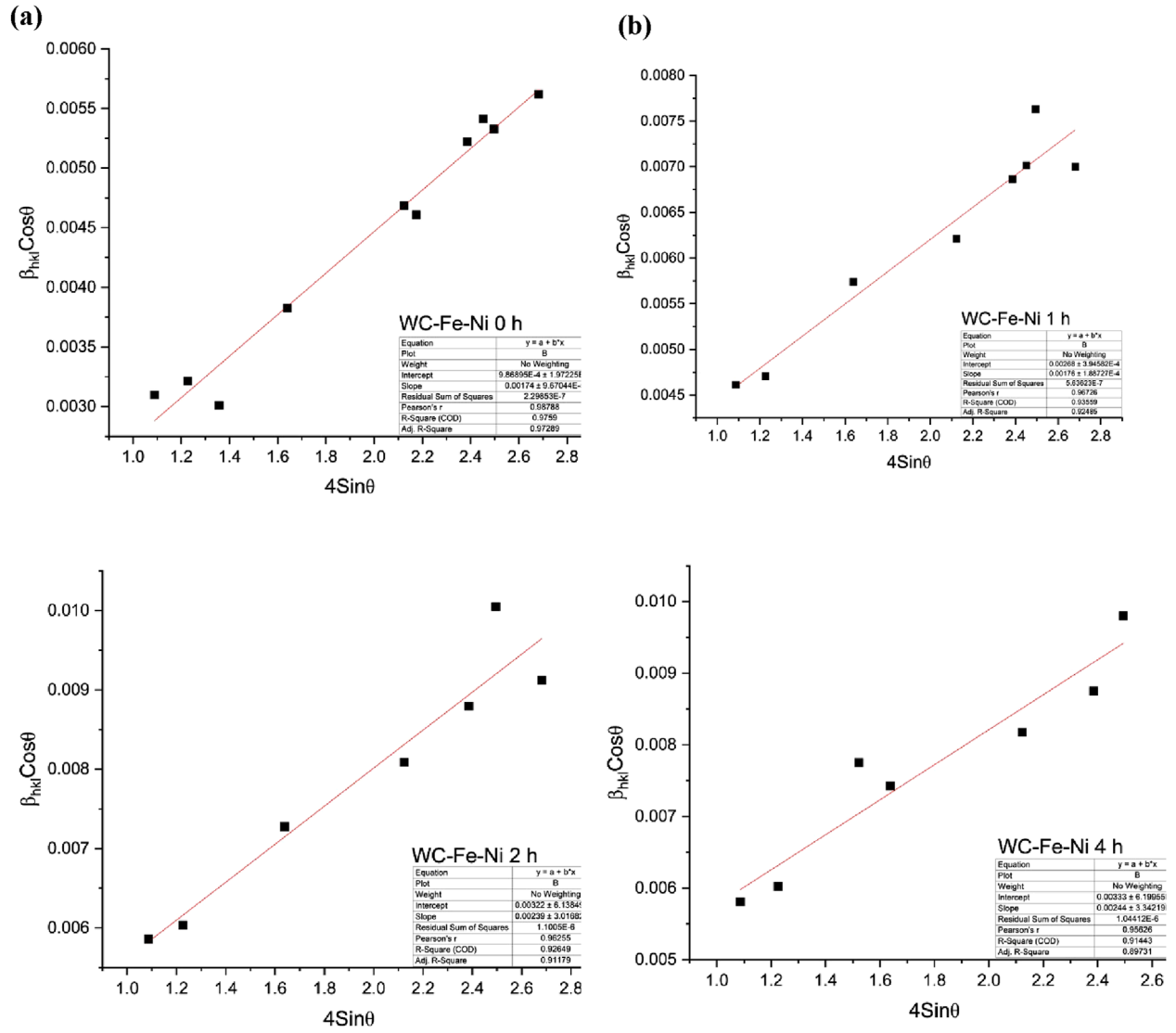

FIGURE 7
Williamson-Hall plots for WC-FeNi powder mixture at different milling times **(a)** 0 h, **(b)** 1 h, **(c)** 2 h, and **(d)** 4 h.

the extensive defect population created by milling facilitates atomic mixing. The literature further indicates that adding Ni to Fe binders stabilizes the γ-austenitic Fe phase (Gibson et al., 2021). Notably, after 4 h only minor evidence of W_2C is observed by XRD. No peaks of Fe_3W_3C carbides or Ni-rich η-type carbides are detected. The Fe-Ni combination thus appears to suppress the formation of discrete η phases during milling, consistent with reports that Fe-Ni binders remain relatively inert toward WC until sintering conditions are attained (Biedma et al., 2024).

Accordingly, the X-ray diffraction data for all three systems reveal a common qualitative scenario. Over the entire 0–4 h interval, the same set of phases is retained, with hexagonal WC dominating and reflections from the metallic binder present; impurity W_2C and W remain at trace levels and show no tendency to grow. In the time-series diffractograms, progressive broadening of WC peaks is accompanied by a moderate decrease in their intensities, indicating a reduction in coherently diffracting domains and an accumulation of microstrain. Williamson-Hall plots consistently show, in all series, an increase in the slope (4ε) and in the intercept (Kλ/D), i.e., a monotonic decrease in crystallite size D and an increase in microstrain ε. This trend is most pronounced for WC-Fe: by 1–2 h the slope rises markedly and the intercept increases, and according to calculations (Table 5) the WC crystallite size D decreases stepwise from 54.5 nm (0 h) to 31.9 nm (1 h) and 25.5 nm (2 h), reaching 22.6 nm at 4 h (Figure 5). Thus, the bulk of nanocrystallization occurs within 0–2 h, while subsequent milling proceeds with diminishing returns against elevated ε.

For WC-Ni (Figure 6), a gentler evolution is observed: WC diffraction peaks broaden less sharply, the Williamson-Hall slope increases smoothly, and the crystallite size *D* decreases from 53.3 nm (0 h) to 24.3 nm (1 h), 23.9 nm (2 h), and 20.7 nm (4 h). The microstrain is lower than in WC-Fe, consistent with the damping role of ductile Ni and the more uniform deformation of WC grains.

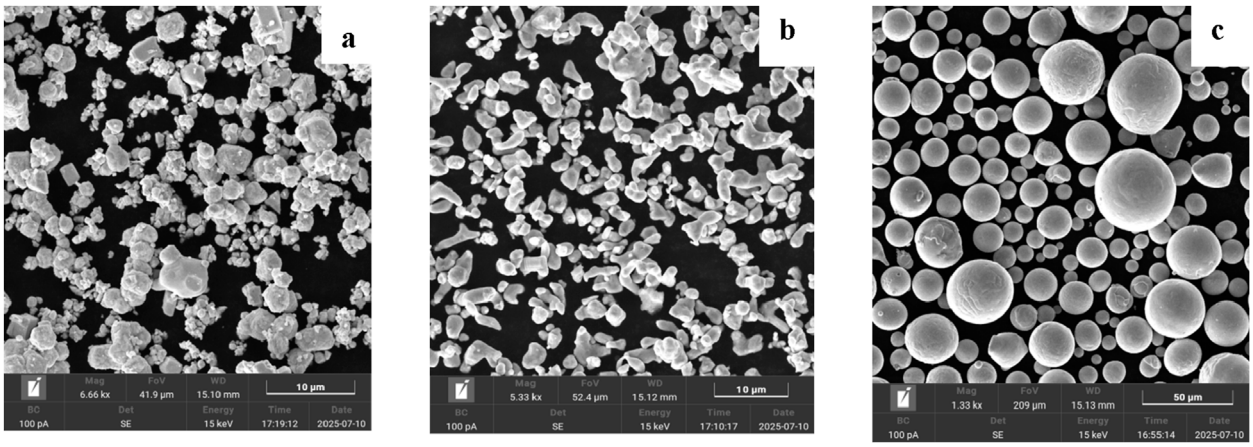

FIGURE 8
SEM images of the initial powders before mechanosynthesis: **(a)** WC; **(b)** Fe; **(c)** Ni.

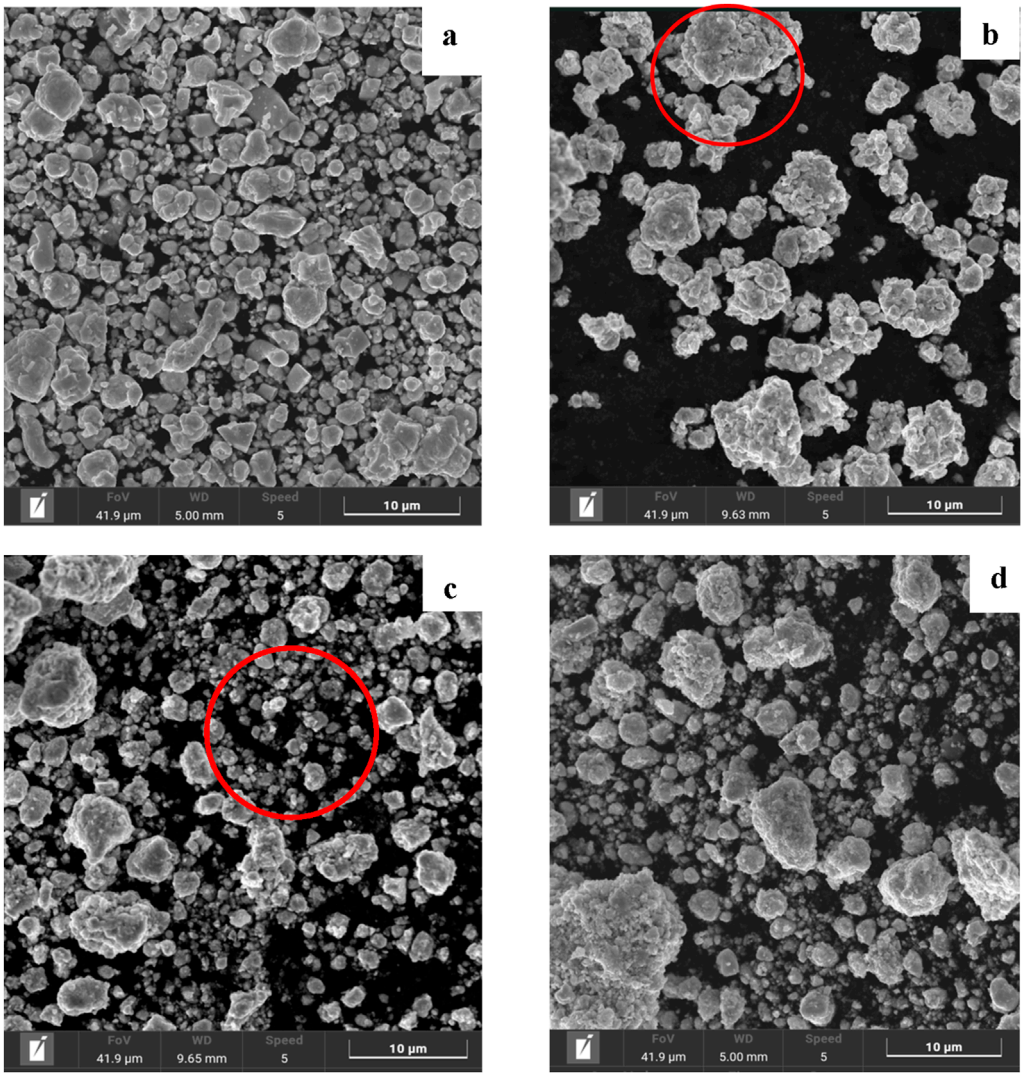

FIGURE 9
SEM images of the 88wt.%WC-12wt% Fe powder mixture subjected to mechanosynthesis at 500 rpm for different durations: **(a)** initial powder mixture; **(b)** after 1 h; **(c)** after 2 h; **(d)** after 4 h.

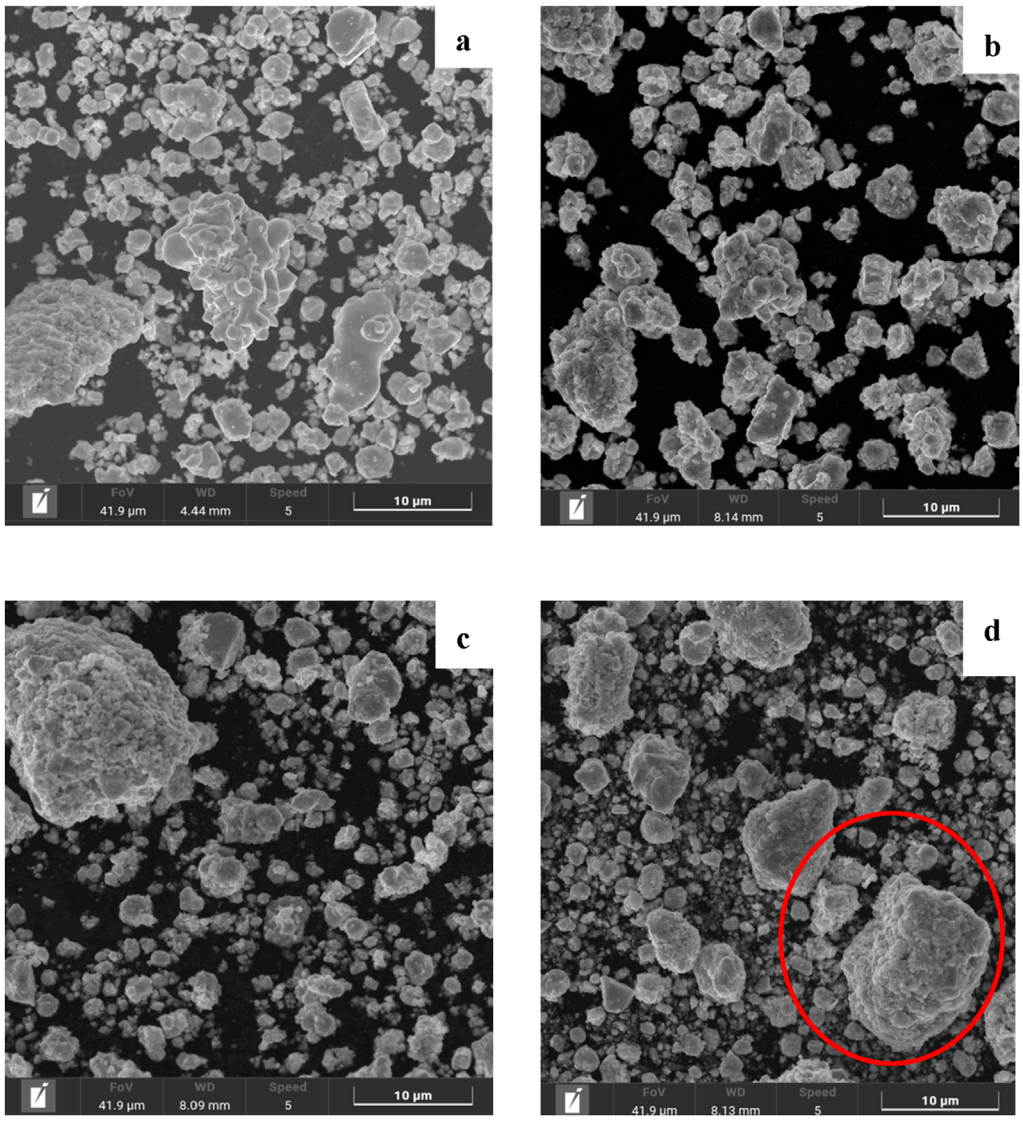

FIGURE 10
SEM images of the 88wt.%WC-12wt.%Ni powder mixture subjected to mechanosynthesis at 500 rpm for different durations: **(a)** initial powder mixture; **(b)** after 1 h; **(c)** after 2 h; **(d)** after 4 h.

In the ternary WC-FeNi system, Williamson–Hall analysis registers an accelerated early reduction in DDD: 51.6 nm (0 h) → 33.6 nm (1 h) → 21.5 nm (2 h), followed by near-saturation at 21.1 nm by 4 h; the W-H slope lies between the Fe-only and Nionly series, i.e., ε increases moderately (Figure 7). Taken together, XRD and Williamson-Hall results show that mechanosynthesis drives the powders into a nanocrystalline WC state with a controlled rise in ε. The best balance rapid early reduction of D under moderate microstrain and without the appearance of new phases is achieved in WC-FeNi, attributable to the formation of a homogeneous Fe(Ni) binder. The WC-Fe series attains the lowest D but is accompanied by higher residual strain/stresses, whereas WC-Ni exhibits the smallest ε with a somewhat slower nanocrystallization rate.

3.2 Microstructural evolution: SEM-EDS analysis

To provide a complete picture of the morphological transformations occurring during mechanosynthesis, Figure 8 presents SEM images of the initial WC, Fe, and Ni powders prior to mechanical activation. These images highlight the distinctive morphology and particle size distribution of each component. WC particles (Figure 5a) appear as irregular agglomerates with faceted surfaces, while Fe particles (Figure 5b) exhibit elongated, fractured shapes typical for ductile deformation. In contrast, Ni powders (Figure 5c) are characterized by nearly perfect spherical morphology, indicating their atomized origin. These initial morphological features play a critical role in governing the

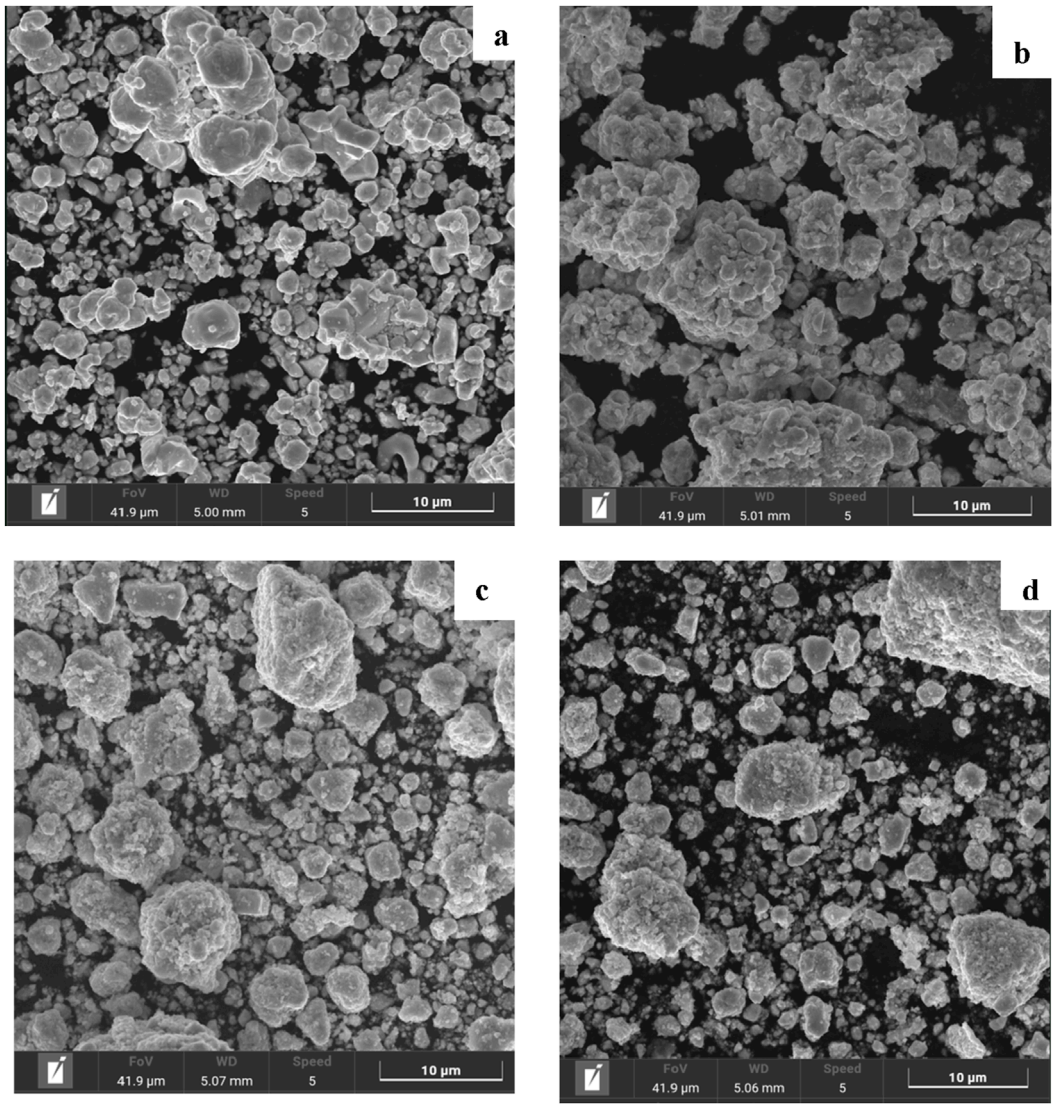

FIGURE 11
SEM images of the 88 wt.%WC-6 wt.%Fe-6 wt.%Ni powder mixture subjected to mechanosynthesis at 500 rpm for different durations: **(a)** initial powder mixture; **(b)** after 1 h; **(c)** after 2 h; **(d)** after 4 h.

subsequent fragmentation, cold welding, and dispersion behavior during high-energy milling.

Figure 9 presents SEM micrographs of WC-Fe after different milling times: (a) as-mixed, (b) 1 h, (c) 2 h, and (d) 4 h. In the unmilled state (Figure 9a), the microstructure is characterized by large, dense agglomerates of WC with smooth surfaces and sparsely distributed fine Fe particles. The blend exhibits high porosity and a lack of interparticle bonding typical of simple mixing. After 1 h (Figure 9b), cold welding appears: the ductile Fe is deformed into flattened lamellae, partially encapsulating WC fragments. This is a characteristic mechanism of mechanical alloying, whereby ductile phases weld while brittle WC fractures and becomes embedded in the metallic matrix. The surfaces become rougher, and defect-like "shear bands" appear, which can facilitate solid-state reactions. After 2 h (Figure 9c), the structure is markedly more homogeneous: intensive comminution produces submicron composite particles with irregular, textured surfaces. The powder consists predominantly of composite platelets in which WC nanograins are embedded in an Fe matrix. After 4 h (Figure 9d), fracture processes begin to dominate: large platelets break down into smaller particles. In WC-Fe milled for 4 h, submicron agglomerates form in which WC nanocrystallites are bonded by Fe. Fe is uniformly distributed around WC grains (a bright matrix surrounding the darker WC), filling the intergranular space. Notably, Fe-bonded particles appear more irregular and porous compared with Ni-bonded particles.

Figure 10 shows the microstructural evolution of WC–Ni. Initially (Figure 10a), the blend consists of WC agglomerates similar to the WC-Fe system. After 1 h (Figure 10b), the agglomerates partially break up, and many WC grains become encapsulated by Ni layers, forming a lamellar composite structure. After 2 h (Figure 10c), these Ni-WC lamellae begin to fragment: work-hardened Ni together with abrasive WC grains induces cracking of the larger layers. By 4 h (Figure 10d), a dispersed powder of

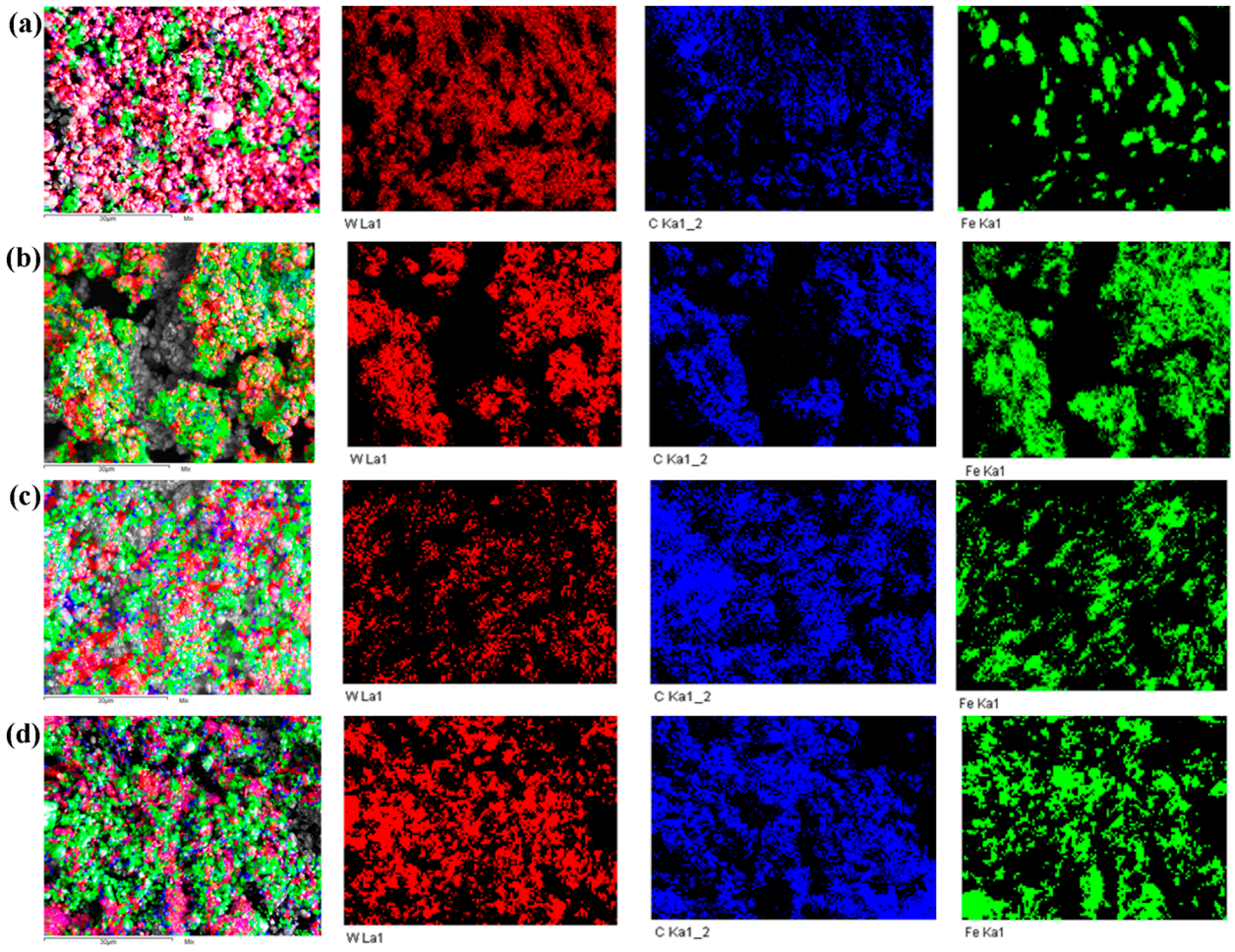

FIGURE 12
SEM-EDS elemental mapping of WC-Fe composite powders after different milling times: **(a)** 0 h, **(b)** 1 h, **(c)** 2 h, **(d)** 4 h.

submicron and micron-sized particles is obtained. However, re-agglomeration is observed: fine particles tend to adhere due to the plasticity of Ni, leading to cold welding. At 4 h, WC–Ni particle surfaces appear smoother and exhibit fewer cracks than in WC–Fe. Overall, Ni promotes homogenization and encapsulation of WC: virtually every WC grain is coated with Ni, forming a "core–shell" morphology, which is favorable for subsequent sintering.

Encapsulation of WC particles, forming a composite microstructure in which each WC grain is likely in close contact with the Ni matrix.

After 1 h of milling, the WC-FeNi powders consist of large, flattened composite particles (as in the Ni-only case), but with a notable distinction: the presence of Fe reduces the excessive plasticity of the Ni lamellae (Figure 11). Platelet-like particles in WC-FeNi at 1–2 h appear somewhat less ductile than in WC-Ni they are more fragmented and not as thin or wide. This indicates joint participation of Fe and Ni in deformation: Ni promotes distribution of the binder, whereas Fe (owing to its higher strength) promotes earlier cracking within Ni-rich platelets. In fact, many WC grains in the 4 h FeNi powder are individually wrapped by a thin Fe–Ni layer, yielding a nanoscale core–shell morphology. This is advantageous for sintering and microstructure control. The mixed-binder powder also exhibits fewer large pores/voids in SEM than the Fe-only powder; the presence of Ni aids binder flow and filling of interparticle gaps during milling. Compared with the Ni-only powder, FeNi particles are slightly smaller and more fractured (because Fe drives greater comminution), resulting in fewer oversized agglomerates. Overall, SEM analysis confirms that combining Fe and Ni provides an optimal balance between cold welding and fragmentation during milling, leading to a highly homogeneous composite powder. Such homogeneity is frequently cited in the literature as a hallmark of Fe-Ni binders, consistent with the present powder-stage observations. SEM indicates that, after milling, this powder attains the most homogeneous microstructure among the three compositions (Williamson and Hall, 1953).

SEM-EDS surface mapping provides key information on mixture homogeneity and agglomeration mechanisms (Figure 12). For the as-received WC-Fe powders, elemental distribution maps show a strong contrast: WC particles contain virtually no iron or nickel, and, conversely, metallic particles contain no tungsten. This confirms that prior to milling the constituents are unevenly distributed and exist as separate entities. After 1 h

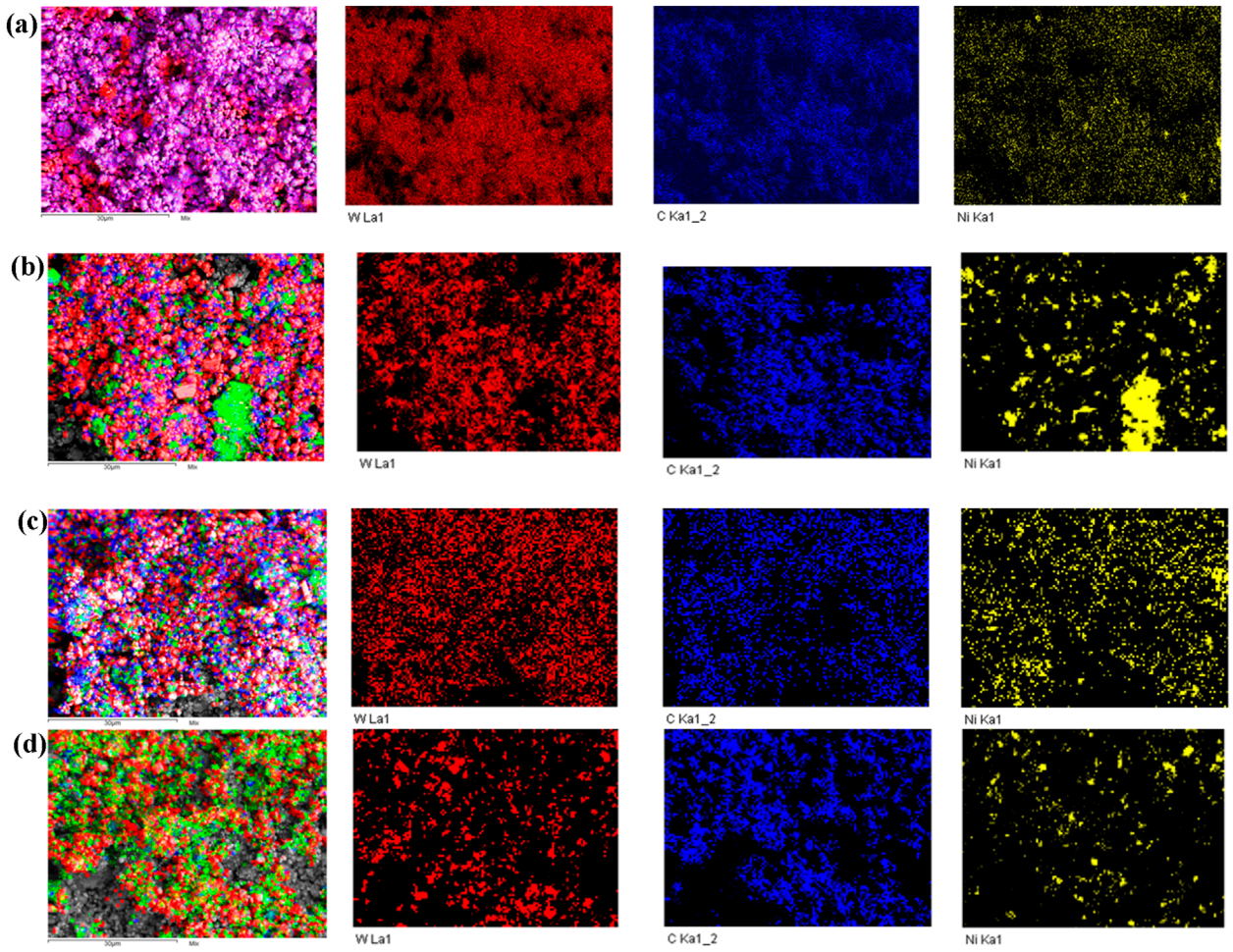

FIGURE 13
SEM-EDS elemental mapping of WC-Ni composite powders after different milling times: **(a)** 0 h, **(b)** 1 h, **(c)** 2 h, **(d)** 4 h.

of mechanosynthesis, the maps reveal the first signs of uniform binder spreading over the particles. In the WC-Fe system, iron begins to coat WC particle surfaces: Fe "spots" appear on the same agglomerates where W is present on the EDS maps. However, the distribution is not yet fully homogeneous; regions with elevated Fe concentration can be distinguished (e.g., in intergranular zones between WC grains where the ductile iron has been extruded).

As the milling time increases to 2 hand especially to 4 h the SEM-EDS maps show an almost complete overlap of the WC and binder signals in all systems. In WC-Ni, likewise, nickel distributes around WC particles (Figure 13). Even at an early stage, Ni tends to form thin interlayers: the Ni maps display a relatively continuous background over agglomerates that also exhibit a W signal, indicating encapsulation ("wrapping") of WC by Ni.

In WC-FeNi samples after 2 h, WC-rich regions are invariably accompanied by a uniform Fe-Ni distribution (Figure 14). No distinct "islands" of pure Ni or Fe are observed indicating that the metallic binder is dispersed throughout the powder and that each agglomerate constitutes a composite particle containing both WC and the metallic phase. This outcome evidences a high degree of homogeneity in the distribution of the alloying elements.

Thus, with increasing mechanosynthesis time, all three compositions undergo a transition from a coarsely dispersed, heterogeneous mixture to a finer, more homogeneous, and mechanically activated powder system. The initial blends are characterized by minimal interaction between constituents and the presence of agglomerates. After just 1 h of processing, agglomerate breakup begins and the particle morphology indicates intensive mechanical action; by 2 h the structure becomes denser and the signatures of interphase interactions are more pronounced.

3.3 Granulometric evolution

The particle-size distribution curves (Figures 15a–c) reveal a bimodal character that becomes more pronounced with increasing milling time. After just 1 h, particle growth is especially evident in WC-Fe: if the initial mean particle size was ~3.4 μm, then after 1 h the D50 reaches ~5.6 μm (Table 6). In the Ni-containing samples (WC-Ni), growth is less pronounced D50 increases from 2.9 to

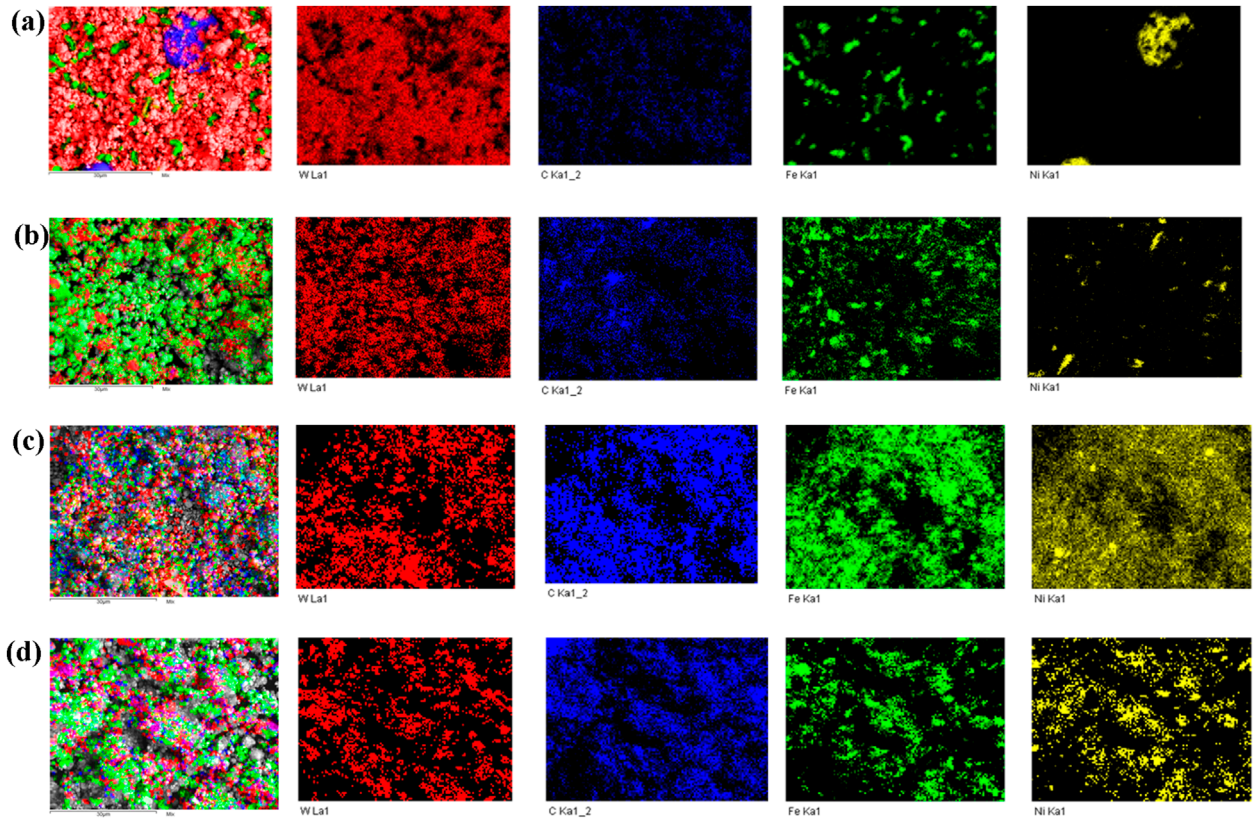

FIGURE 14
SEM-EDS elemental mapping of WC-FeNi composite powders after different milling times: **(a)** 0 h, **(b)** 1 h, **(c)** 2 h, **(d)** 4 h.

4.0 μm in 1 h indicating differences in plasticity and agglomeration tendency between iron and nickel. As mechanosynthesis proceeds, the cumulative curves shift to the right, and the differential histograms show both an increasing fraction and a peak shift of the coarse population.

For all systems, two characteristic particle fractions are clearly expressed after 4 h: (1) fine particles in the submicron to ~1 μm range, corresponding either to individual WC grains (remaining unbonded) or to fragments detached from agglomerates; and (2) large agglomerates of 5–10 μm formed by cold welding. Some bimodality is already discernible in the as-received state, particularly in WC-FeNi, where the starting Fe particles were larger than the WC particles, producing two distribution peaks. The initial D50 is 4.11 μm, increasing to 5.44 μm (1 h), 6.13 μm (2 h), and 7.42 μm (4 h). As seen in Figure 15c, the particle-size growth is less intense than in WC-Fe but greater than in WC-Ni. The distribution pattern indicates partial structural stabilization due to synergy within the binder: Fe enhances interfacial bonding, whereas Ni provides plasticity and mitigates excessive agglomeration. Formation of fine aggregates is observed after 2 h, but by 4 h the distribution widens a sign of secondary aggregation onset.

The PSD data are consistent with the SEM images. In the initial samples, isolated particles and a small number of weakly bonded conglomerates predominate; with increasing processing time, the fraction of multigrain composite aggregates increases steadily, with characteristic sizes falling within the range of the right-hand modal peak of the volume-weighted distribution. A numerically small but volume-dominant family of large particles clearly visible even at low magnification forms the right "tail" of the PSD and drives the shift of the volume-weighted median D50. By contrast, number-weighted interpretation of the SEM images naturally emphasizes the fine fraction, biasing the visual impression toward smaller sizes.

At first glance, the results appear contradictory: as mechanosynthesis proceeds, the average particle (agglomerate) size increases, whereas the characteristic crystallite size of WC within the particles decreases. This contradiction is only apparent because different structural length scales are being considered. High-energy ball milling involves a competition between two processes fracture (comminution) and cold welding (agglomeration). At the early stages, fracture dominates: large agglomerates are broken into smaller fragments by ball impacts. As a plastic metallic phase accumulates on particle surfaces and the hard grains become finer, the role of cold welding increases: particles begin to adhere, forming new agglomerates. Nevertheless, simultaneous with the coarsening of agglomerates, fragmentation at the nanoscale intensifies: within each large agglomerate, WC crystallites are broken up, accumulate dislocations, and shrink under repeated impacts. Thus, the extending HEBM to ~2 h is justified by mechanistic and quantitative outcomes. Between 1 h and 2 h, oxide disruption, defect accumulation, and short-range Fe/Ni interdiffusion become pronounced, as indicated by the disappearance/merging of Ni/Fe reflections and a marked reduction of WC crystallite size, which

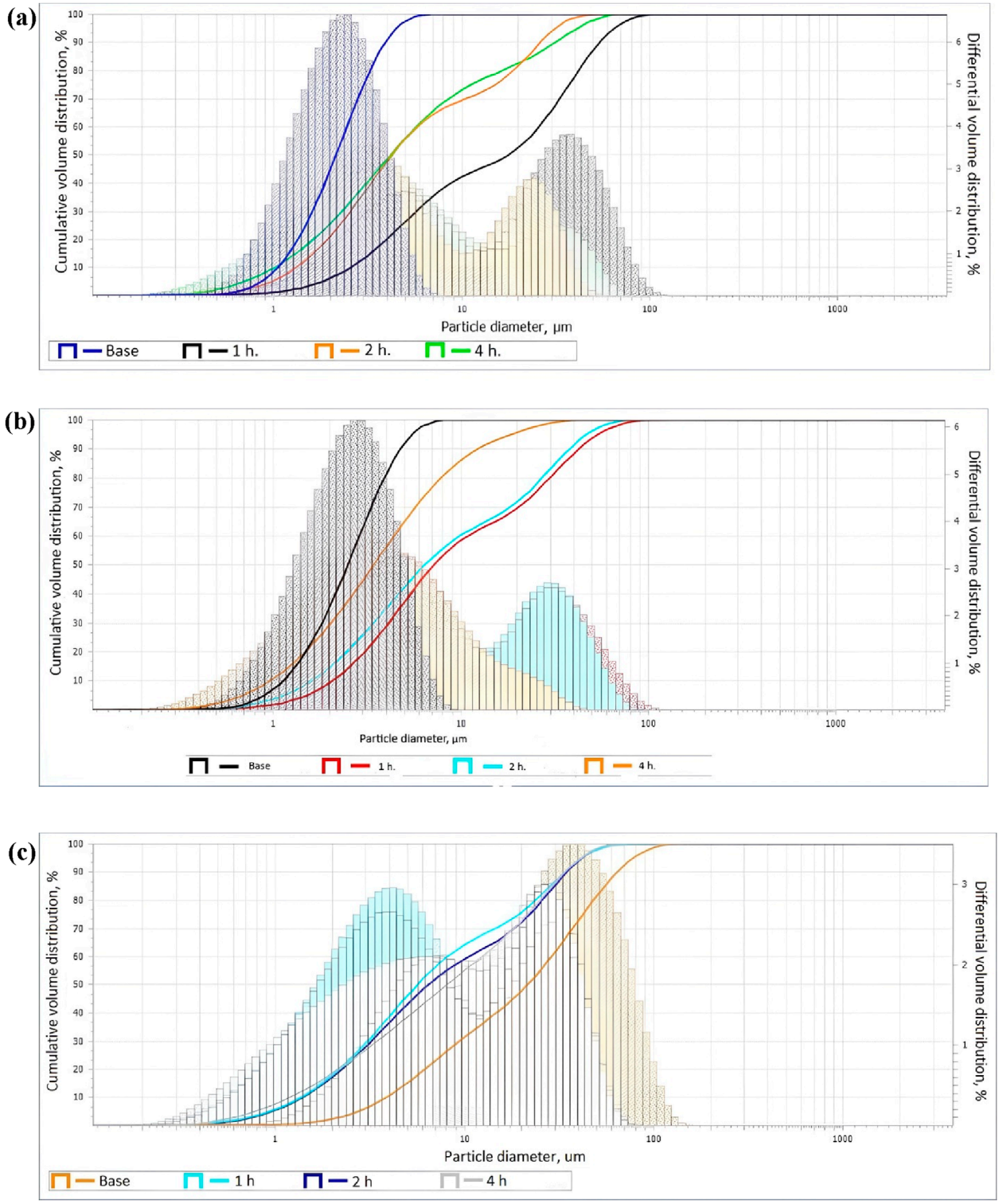

FIGURE 15
Bimodal particle size distribution of the system after 0, 1, 2, and 4 h of mechanosynthesis: **(a)** 88 wt% WC-12 wt% Fe; **(b)** 88 wt% WC-12 wt% Ni; **(c)** 88 wt% WC-6 wt% Fe-6 wt% Ni.

improves subsequent sinterability and microstructural control. Beyond 2 h, the incremental refinement is while cold-welding drives particle-scale coarsening that degrades powder processability. Because milling energy scales approximately with time, the energy cost of 4 h yields diminishing returns relative to 2 h. Accordingly, an energy-efficient processing window of 1–2 h is identified; the 4 h condition is retained only as a mechanistic upper bound to evidence the plateau and agglomeration.

TABLE 6 Average particle sizes (D_{50}) of composite powders depending on milling time.

Sample	initial powder mixture	1 h	2 h	4 h
88 wt% WC-12 wt% Fe	3.40 μm	5.63 μm	6.36 μm	10.3 μm
88 wt% WC-12 wt% Ni	2.87 μm	4.00 μm	5.50 μm	7.27 μm
88 wt% WC-6 wt% Fe-6 wt% Ni	4.11 μm	5.44 μm	6.13 μm	7.42 μm

4 Conclusion

The study showed that over 0–4 h of mechanosynthesis the phase constitution in all three systems remained stable: WC and the metallic binder were consistently detected, whereas secondary phases W_2C and W did not exceed trace levels (<1%). In WC-FeNi, a decrease in free Ni from 1.9% to 0.5% and an increase in Fe from 9.5% to 23.6% were recorded, indicating the formation of an Fe(Ni) solid solution already during milling. Williamson-Hall analysis revealed that the WC crystallite size decreased from the initial ~50–55 nm to 22.6 nm (WC-Fe), 20.7 nm (WC-Ni), and 21.1 nm (WC-FeNi) after 4 h of processing. The principal reduction occurred within 0–2 h; for example, in WC-Fe the crystallite size *D* fell from 54.5 to 25.5 nm, i.e., by more than a factor of two. Microstrain increased with milling time, reaching the highest level in WC-Fe, an intermediate level in WC-FeNi, and the lowest in WC-Ni. In parallel, the volume-weighted particle size (D50) increased due to cold welding and aggregation: from 3.40 to 10.30 μm in WC–Fe, from 2.87 to 7.27 μm in WC-Ni, and from 4.11 to 7.42 μm in WC-FeNi. SEM corroborated the growth of multigrain composite aggregates specifically in the 5–15 μm range corresponding to the right-hand mode of the PSD. Thus, an inverse correlation between nano- and micro-scales was established: particles coarsened while the WC crystallites within them were refined to ~20–23 nm. Comparison of the three systems showed that WC-Fe yields the greatest crystallite-size reduction but is accompanied by the largest increases in D50 and microstrain. WC-Ni exhibits the lowest εεε and moderate particle coarsening, but somewhat gentler crystallite-refinement kinetics. The most balanced response is provided by WC-FeNi: a crystallite size of ~21 nm combined with D50 ≈ 7.4 μm and moderate microstrain, making it optimal for subsequent uniform sintering. The limitation of the study is that the results presented refer to the pre-sintering state of the powders and record structural evolution only at the mechanosynthesis stage. Although recrystallization or binder redistribution may occur during subsequent sintering, it is the initial powder state that determines their sintering activity and largely defines the final properties of the material.

Data availability statement

The original contributions presented in the study are included in the article/supplementary material, further inquiries can be directed to the corresponding author.

Author contributions

MA: Conceptualization, Project administration, Writing – review and editing. SK: Conceptualization, Visualization, Writing – original draft, Writing – review and editing. AK: Conceptualization, Investigation, Writing – original draft, Writing – review and editing. AU: Funding acquisition, Writing – original draft. LB: Funding acquisition, Writing – original draft. MR-G: Investigation, Visualization, Writing – review and editing. YA: Funding acquisition, Validation, Writing – review and editing.

Funding

The author(s) declare that financial support was received for the research and/or publication of this article. This research is funded by the Committee of Science of the Ministry of Science and Higher Education of the Republic of Kazakhstan (grant No. BR24992925).

Acknowledgments

We express our gratitude to the Science Committee of the Ministry of Science and Higher Education of the Republic of Kazakhstan. For support of the project "Development of technologies and materials for innovative development of the manufacturing industry of the Republic of Kazakhstan".

Conflict of interest

Authors SK and YA were employed by LLP "Institute of Innovative Technologies and New Materials".

The remaining authors declare that the research was conducted in the absence of any commercial or financial relationships that could be construed as a potential conflict of interest.

Generative AI statement

The author(s) declare that no Generative AI was used in the creation of this manuscript.

Any alternative text (alt text) provided alongside figures in this article has been generated by Frontiers with the support of artificial intelligence and reasonable efforts have been made to ensure accuracy, including review by the authors wherever possible. If you identify any issues, please contact us.

Publisher's note

References

Abbasi, M., Tahaei, A., Bagheri Vanani, B., and Arizmendi-Morquecho, A. (2024). Adding WC nano-particles to nickel-based coating deposited by PTA process: microstructure and nanoindentation hardness characteristics. *JOM* 76 (8), 4235–4248. doi:10.1007/s11837-024-06666-4

Biedma, Á., Sánchez, G., de Nicolás, M., Bertalan, C., Useldinger, R., Llanes, L., et al. (2024). A comparative study on the wear performance and high-temperature oxidation of Co-Free cermets and hardmetals. *Materials* 17, 3615. doi:10.3390/ma17143615

Cramer, C. L., Shichalin, O. O., and Papynov, E. K. (2020). WC-Based alloys with Fe/Ni matrix: microstructure and mechanical properties. *Int. J. Refract. Met. Hard Mater.* 92, 105280. doi:10.1016/j.ijrmhm.2020.105280

Cullity, B. D. (1986). *Elements of X-ray diffraction (2nd ed)*. Reading, MA: Addison-Wesley.

Fathipour, Z., Javanbakht, M., Rezaei, M., Karimzadeh, F., Rauf, A., and Akbarzadeh, A. (2024). Effect of binder on oxidation properties of tungsten carbides: a review by a conceptual classification approach. *Ceramics* 7 (1), 166–191. doi:10.3390/ceramics7010011

Gao, Y., Gao, K., Fan, L., Yang, F., Guo, X., Zhang, R., et al. (2020). Oscillatory pressure sintering of WC–Fe–Ni cemented carbides. *Ceram. Int.* 46 (8), 12727–12731. doi:10.1016/j.ceramint.2020.02.040

García, J., Blomqvist, A., Llanes, L., and Kaplan, B. (2019). Cemented carbide microstructures: a review. *Int. J. Refract. Met. Hard Mater.* 80, 40–68. doi:10.1016/j.ijrmhm.2018.12.004

Gibson, I., Rosen, D. W., Stucker, B., Rosen, D., Stucker, B., Khorasani, M., et al. (2021). "Additive manufacturing technologies,", 17. Cham, Switzerland: Springer, 160–186. doi:10.1007/978-3-030-56127-7

Gruber, P. H., Katea, S. N., Westin, G., and Akhtar, F. (2023). WC–Ni cemented carbides prepared from Ni nano-dot coated powders. *Int. J. Refract. Met. Hard Mater.* 117, 106375. doi:10.1016/j.ijrmhm.2023.106375

Hoier, P., Klement, U., Alagan, N. T., Beno, T., and Wretland, A. (2017). Characterization of tool wear when machining alloy 718 with high-pressure cooling using conventional and surface-modified WC–Co tools. *J. Superhard Mater.* 39, 178–185. doi:10.3103/S1063457617030054

Jayaraj, J., Elo, R., Surreddi, K. B., and Olsson, M. (2023). Electrochemical and passivation behavior of a corrosion-resistant WC–ni(W) cemented carbide in synthetic mine water. *Int. J. Refract. Met. Hard Mater.* 114, 106227. doi:10.1016/j.ijrmhm.2023.106227

Krawitz, A., and Drake, E. (2015). Residual stresses in cemented carbides—an overview. *Int. J. Refract. Met. Hard Mater.* 49, 27–35. doi:10.1016/j.ijrmhm.2014.07.018

Kumar, R., Kariminejad, A., Antonov, M., Goljandin, D., Klimczyk, P., and Hussainova, I. (2023). Progress in sustainable recycling and circular economy of tungsten carbide hard metal scraps for industry 5.0 and onwards. *Sustainability* 15 (16), 12249. doi:10.3390/su151612249

Lantcev, E., Nokhrin, A., Malekhonova, N., Boldin, M., Chuvil'deev, V., Blagoveshchenskiy, Y., et al. (2021). A study of the impact of graphite on the kinetics of SPS in Nano- and submicron WC-10% Co powder compositions. *Ceramics* 4, 331–363. doi:10.3390/ceramics4020025

Lantsev, E. A., Malekhonova, N. V., Nokhrin, A. V., Chuvil'deev, V. N., Boldin, M. S., Andreev, P. V., et al. (2021). Spark plasma sintering of fine-grained WC hard alloys with ultra-low cobalt content. *J. Alloys Compd.* 857, 157535. doi:10.1016/j.jallcom.2020.157535

Li, H., Zhang, H., and Jiang, Z. (2024). Investigation of the effect of partial Co substitution by Ni and Fe on the interface bond strength of WC cemented carbide based on first-principles calculations. *Mater. Today Commun.* 40, 109470. doi:10.1016/j.mtcomm.2024.109470

Lima, M. J., Silva, F. E., Raimundo, R. A., Vitoriano, J. O., Lourenço, C. S., Morales, M., et al. (2024). Enhanced properties of hard metal WC-Ni processed from nanostructured powders. *Ceram. Int.* 50 (22), 47445–47455. doi:10.1016/j.ceramint.2024.09.096

Lyu, X., Jiang, X., Sun, H., and Shao, Z. (2020). Microstructure and mechanical properties of WC–Ni multiphase ceramic materials with $NiCl_2$•$6H_2O$ as binder. *Nanotechnol. Rev.* 9 (1), 543–557. doi:10.1515/ntrev-2020-0044

Ravotti, D. A. S., Correas, H. M., and Luis, N. C. (2024). Last decade insights on cemented carbides: a review on alternative binders, new consolidation techniques and advanced characterization. *Eclética Quím.* 49. doi:10.26850/1678-4618.eq.v49.2024.e1529

Rong, H., Wang, X., Zhang, T., and Zhao, H. (2012). Ultrafine WC-Ni cemented carbides fabricated by spark plasma sintering. *Mater. Sci. Eng. A* 532, 543–547. doi:10.1016/j.msea.2011.10.119

Scherrer, P. (1918). Göttinger nachrichten math. *Phys* 2, 98–100.

Shichalin, O. O., Buravlev, I. Y., Papynov, E. K., Golub, A., Belov, A., Buravleva, A., et al. (2020). Comparative study of WC-Based hard alloys fabrication via spark plasma sintering using Co, Fe, Ni, Cr, and Ti binders. *Int. J. Refract. Met. Hard Mater.* 102, 105725. doi:10.1016/j.ijrmhm.2021.105725

Smetanina, K. E., Andreev, P. V., Lantsev, E. A., Nokhrin, A. V., Murashov, A. A., Isaeva, N. V., et al. (2023). Nonuniform distribution of crystalline phases and grain sizes in the surface layers of WC ceramics produced by spark plasma sintering. *Coatings* 13 (6), 1051. doi:10.3390/coatings13061051

Steinlechner, R., de Oro Calderon, R., Koch, T., Linhardt, P., and Schubert, W. D. (2022). A study on WC–Ni cemented carbides: constitution, alloy compositions and properties, including corrosion behaviour. *Int. J. Refract. Met. Hard Mater.* 103, 105750. doi:10.1016/j.ijrmhm.2021.105750

Sten, S., Odqvist, J., Norgren, S. M., and Hedström, P. (2025). Functional-gradient WC-TiC cemented carbides with alternative binders (ni and fe). *Int. J. Refract. Met. Hard Mater.* 131, 107214. doi:10.1016/j.ijrmhm.2025.107214

Sun, J., Zhao, J., Huang, Z., Yan, K., Shen, X., Xing, J., et al. (2020). A review on binderless tungsten carbide: development and application. *Nanomicro Lett.* 12, 13. doi:10.1007/s40820-019-0346-1

Tahaei, A., Vanani, B. B., Abbasi, M., and Arizmendi-Morquecho, A. (2023). A different attempt to investigate the influence of PTA parameters on microstructure evolution and mechanical characteristics of nickel base powder (Ni-WC) deposited tool steel. *J. Mater. Res. Technol.* 27, 7970–7985. doi:10.1016/j.jmrt.2023.11.230

Tahaei, A., Vanani, B. B., Abbasi, M., and Arizmendi-Morquecho, A. (2024). The hardfacing properties of the nickel-based coating deposited by the PTA process with the addition of wc nano-particles: wear investigation. *Tribol. Int.* 193, 109472. doi:10.1016/j.triboint.2024.109472

Williamson, G. K., and Hall, W. H. (1953). X-ray line broadening from filed aluminium and wolfram. *Acta metall.* 1 (1), 22–31. doi:10.1016/0001-6160(53)90006-6

Yang, Y., Zhang, C., Wang, D., Nie, L., Wellmann, D., and Tian, Y. (2020). Additive manufacturing of WC-Co hardmetals: a review. *Int. J. Refract. Met. Hard Mater.* 108, 1653–1673. doi:10.1007/s00170-020-05389-5

Zeiler, B. (2019). "Tungsten and cobalt, the two key elements of the hardmetal industry," in *11th int. Conf. Sci. Hard mater., khao Lak*.